



OPEN

Persistent impact of Fukushima decontamination on soil erosion and suspended sediment

Bin Feng ¹, Yuichi Onda ¹✉, Yoshifumi Wakiyama ², Keisuke Taniguchi ³, Asahi Hashimoto ¹ and Yupan Zhang¹

In Fukushima, government-led decontamination reduced radiation risk and recovered ¹³⁷Cs-contaminated soil, yet its long-term downstream impacts remain unclear. Here we provide the comprehensive decontamination impact assessment from 2013 to 2018 using governmental decontamination data, high-resolution satellite images and concurrent river monitoring results. We find that regional erosion potential intensified during decontamination (2013–2016) but decreased in the subsequent revegetation stage. Compared with 2013, suspended sediment at the 1-year-flood discharge increased by 237.1% in 2016. A mixing model suggests that the gradually increasing sediment from decontaminated regions caused a rapid particulate ¹³⁷Cs decline, whereas no significant changes in downstream discharge-normalized ¹³⁷Cs flux were observed after decontamination. Our findings demonstrate that upstream decontamination caused persistently excessive suspended sediment loads downstream, though with reduced ¹³⁷Cs concentration, and that rapid vegetation recovery can shorten the duration of such unsustainable impacts. Future upstream remediation should thus consider pre-assessing local natural restoration and preparing appropriate revegetation measures in remediated regions for downstream sustainability.

Radioactive material leakage from nuclear industry activities or nuclear accidents poses a major threat to the environment and the economy^{1,2}. Historically, widespread radioactive contamination has been observed several times, such as the Kyshtym accident (Soviet Union) in the 1940s–50s³, Windscale accident (England) in 1957 (ref. ⁴) and Chernobyl accident (Soviet Union) in 1986 (ref. ⁵). Long-term radiation exposure and radiophobia have increased the health risk and psychological pressure on the people of these regions, resulting in the abandonment of large areas rich in environmental resources and consequently in constrained sustainable human development^{6,7}. As a key means for recovering contaminated regions, mechanical decontamination has been implemented in many legacy sites, including Hanford (United States)⁸ and Chernobyl⁹. However, almost all attention has been directed to understanding in situ decontamination effects^{10,11} and atmospheric particle resuspension issues¹² and little is known about if these perturbations would have secondary environmental impacts on their downstream catchments for the long-term.

On 11 March 2011, the most recent large-scale nuclear accident happened at the Fukushima Daiichi Nuclear Power Plant (FDNPP), Japan¹³. Over 2.7 PBq of fallout ¹³⁷Cs (half-life $T_{1/2} = 30.1$ yr) from the FDNPP was deposited in the terrestrial environment, causing long-term radioactive contamination on large-scale neighbouring catchments^{13,14}. To recover contaminated soil and decrease the exposure dose in Fukushima, the Japanese government evacuated the residents in 2011 and large-scale decontamination was implemented in contaminated villages^{15,16} in 2012. Within a few years, dramatic land-cover changes occurred in the agricultural regions where 5 cm of the surface soil and vegetation were removed and replaced with uncontaminated soil (Fig. 1), with the subsequent natural restoration promoting revegetation in these decontaminated regions^{11,13,16}.

The effectiveness of such intensive decontamination at reducing radiation exposure in situ is apparent, with air dose rates decreasing

by 20–70% after decontamination¹³. However, as ¹³⁷Cs can firmly bind to clay minerals, it is transported along with suspended sediments (particulate ¹³⁷Cs) in the river system to the Pacific Ocean^{17,18}. Comprehensively assessing the impacts of land-use changes in decontaminated regions on the downstream ecosystem is also necessary from the perspective of environmental sustainability. Moreover, recent studies have shown notable differences in the reduction in the particulate ¹³⁷Cs concentration over time across 30 rivers in Fukushima^{19,20}, further underscoring the need to study land-use impacts on downstream particulate ¹³⁷Cs discharge into the ocean.

In addition to contaminant migration, land-use changes induced by strong perturbations (for example, decontamination) also alter land–ocean sediment transfer patterns^{21,22}, which in turn affect elemental cycles²³, biodiversity²⁴ and global climate²⁵. Systematically assessing the perturbations' impacts on downstream river suspended sediments (SS) has thus become a joint goal of many related disciplines and a key part of developing science-based catchment management strategies^{26–29}. However, owing to the limited availability of reliable and concurrent river monitoring data, how downstream river SS variations and land-use changes are linked remains unclear²¹.

With approximately 11.9% of the watershed area subjected to government-led decontamination between 2013 and early 2017, the Niida River Basin in Fukushima (Fig. 2a)^{11,30} provides an excellent opportunity to examine the long-term impact on the dynamics of SS and particulate ¹³⁷Cs in river systems. Previous short-term river studies^{19,20,31–34} have suggested an increased river SS load and decreased particulate ¹³⁷Cs concentrations during decontamination. Several studies that analysed geochemical fingerprints in deposited sediments have implied a significant contribution of sediment sources from the decontaminated regions to the river^{35–37}. Yet, given that threats to sustainable catchment management from anthropogenic perturbations are often long-term^{28,29}, more comprehensive

¹Center for Research in Isotopes and Environmental Dynamics, University of Tsukuba, Tsukuba, Japan. ²Institute of Environmental Radioactivity, Fukushima University, Fukushima, Japan. ³National Institute of Technology, Tsuyama College, Tsuyama, Japan. ✉e-mail: onda@geoenv.tsukuba.ac.jp



Fig. 1 | Decontamination work in agricultural land. **a,b**, Photographs taken during decontamination in Kawamata Town on 4th April 2014 (**a**) and 8th November 2014 (**b**). **c,d**, Photographs taken after decontamination in Iitate Village on 8th April 2015.

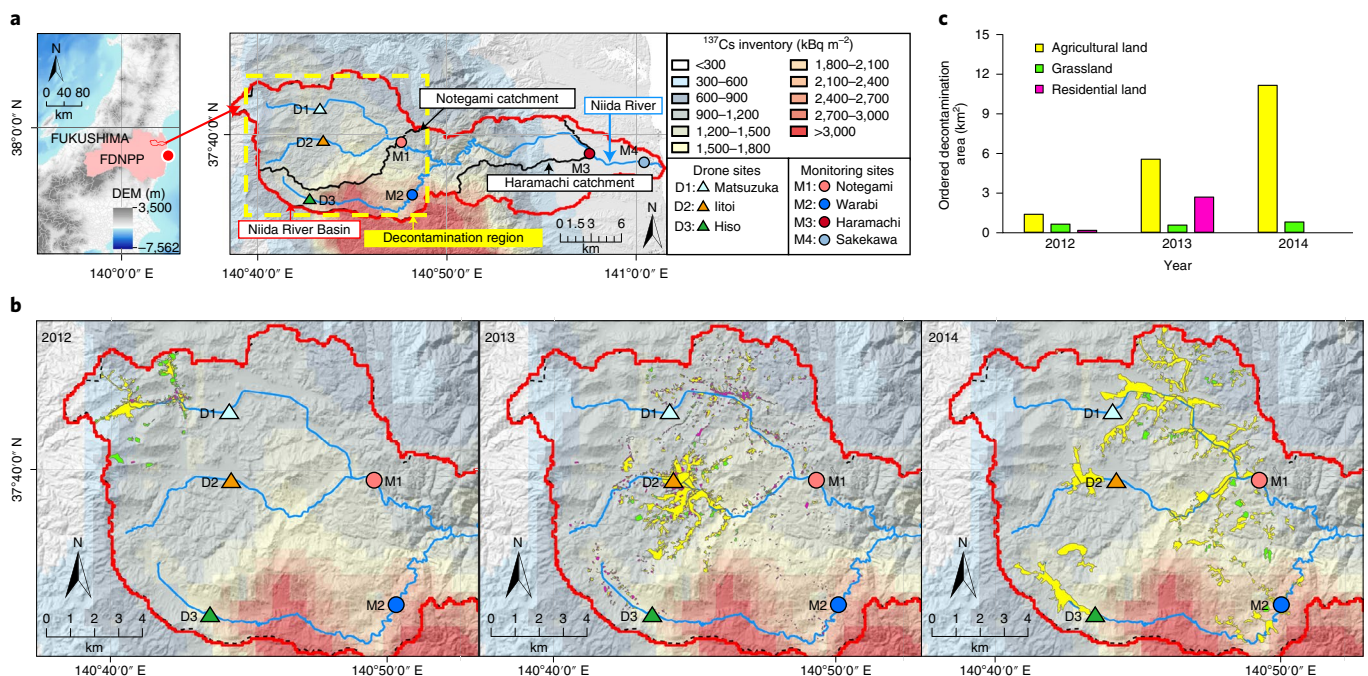


Fig. 2 | Geographic information and decontamination situation in the Niida River Basin. **a**, Study area with ¹³⁷Cs inventory and sites. **b**, Ordered decontamination regions in 2012, 2013 and 2014. Coloured areas in **b** are the same as in **c**. The red line and dashed black line are the boundaries of Niida river basin and Haramachi catchment, respectively. **c**, Ordered decontaminated area for agricultural land (including paddy field and cropland), residential land and grassland, by year. The digital elevation model (DEM) data were from the Geospatial Information Authority of Japan. The ¹³⁷Cs inventory data were obtained from Kato et al.¹⁴. The information for the scheduled decontamination regions (paper maps) was obtained from the Ministry of the Environment of Japan.

and reliable data on quantified land cover and continuous river records are required to explore the effect of decontamination on river SS and particulate ^{137}Cs discharge.

Here we provide a comprehensive assessment of the impacts of land-use changes in decontaminated regions on river SS and particulate ^{137}Cs dynamics, as well as the downstream discharge. We mapped the evolution of decontaminated region boundaries using governmental decontamination documents (Fig. 2b), photographed the land cover in the decontaminated regions using drones and quantified the land-use changes using the normalized difference vegetation index (NDVI) at 10 m spatial resolution. Meanwhile, we conducted a long-term field investigation (Methods and Supplementary Table 1) spanning the decontamination (2013–2016) and natural restoration (2017–2018) stages to continuously record the fluctuations in water discharge and turbidity (10 min temporal resolution) and particulate ^{137}Cs concentrations, both upstream and downstream. Combining the above quantitative data, we systematically reveal that long-term land-use changes in upstream decontaminated regions greatly affect sediment and ^{137}Cs discharge from downstream river systems into the Pacific Ocean.

Land-cover changes in decontaminated regions

Regional decontamination was accomplished in March 2017, spanning over 22.9% and 11.9% of the upstream (Notegami) and downstream (Haramachi) watershed areas, respectively (Fig. 2c). In 2014, agricultural land (18.02 km²) was one of the major land uses in the regions where decontamination was ordered, with a significant increase of over 720% compared with that in 2012. Conversely, the changes in the ordered grassland (1.93 km²) were minimal, with an approximately 26% increase between 2012 and 2014. Given that overall land-cover changes were more pronounced in agricultural lands than in grasslands or residential lands, large-scale agricultural land decontamination may severely alter landscape erodibility and consequently the sediment supply. Moreover, the proximity of the decontaminated agricultural land to rivers increases sediment transport from terrestrial environments.

Drone photographs (Fig. 3a and Supplementary Fig. 1) showed significant land-cover changes in the upstream decontaminated regions. For instance, the agricultural land at the Hiso site (D3, Fig. 3a) was almost bare in August 2016 when the decontamination was completed. However, natural restoration caused the recovery of vegetation during the post-decontamination stage (August 2018). Considering the decontamination sequence and seasonal dependence of the plant growth cycle³⁸, drastic spatiotemporal land-cover changes in the decontamination regions are conceivable.

To quantitatively estimate and compare land-cover changes in the decontaminated regions, we generated NDVI maps in these regions based on the available satellite images from Sentinel 2 and the Moderate Resolution Imaging Spectroradiometer (MODIS) between 2011 and 2018. The comparison between realistic scenarios and Sentinel 2-based NDVI maps (spatial resolution: 10 m) from drone observation sites (Fig. 3a and Supplementary Fig. 1) confirmed the feasibility of NDVI images in distinguishing bare land and agricultural land with vegetation cover. To improve the temporal–spatial resolution of the NDVI dataset, we used the enhanced spatial and temporal adaptive reflectance fusion model (ESTARFM)³⁹ to fuse Sentinel 2 and MODIS maps. Subsequently, we used interpolation to link these newly generated NDVI data (spatial resolution: 10 m) and plotted daily NDVI variations for all decontaminated regions between 2011 and 2018 (Fig. 3b).

In the daily NDVI variation curve, the peak NDVI during 2013–2014 was similar to the pre-decontamination stage (2012) but decreased by approximately 10% in 2016. After decontamination, the peak value presented an increasing trend under the influence of

vegetation recovery. However, as the government lifted the evacuation zone after 2017 and allowed the residents to return, vegetation was again removed from some areas planned for agricultural activities in 2018 (Supplementary Fig. 1b). Further analyses of the NDVI variations in the decontaminated regions scheduled in 2012 (Fig. 3c), 2013 (Fig. 3d) and 2014 (Fig. 3e) showed that the NDVI peaks were decreased by approximately 12%, 11% and 15%, respectively, within 2–3 years after decontamination was ordered, thereby providing unambiguous evidence for decreasing vegetation land cover caused by decontamination.

We converted all NDVI maps derived from ESTARFM-images to $C \times P$ (cover management and support practice factors, respectively) maps using empirical models^{40,41}. We then estimated erosion potential (that is, $K \times LS \times C \times P$ in the revised Universal Soil Loss Equation (RUSLE); Methods) maps using the LS (slope length and slope steepness factors, respectively) map (Supplementary Fig. 2) and K (soil erodibility) factor in the decontaminated regions. We found that the slopes of decontaminated regions were generally similar for each decontamination-ordered year (Supplementary Fig. 2), suggesting that the erosion potential was consistent with the NDVI in the decontaminated regions. Therefore, we also estimated the daily variation curve of the erosion potential using the mean CP , LS and K factors in the decontaminated regions.

Here we show the ESTARFM-based NDVI (Fig. 3f) and erosion potential (Fig. 3g) during the summer season for each year (specific periods in Supplementary Table 2). NDVI showed a decreasing trend from 2013 to 2016, while the erosion potential peaked in 2016, representing approximately 98% and 52% increases over the pre-decontamination (2011) and natural restoration (2018) stages, respectively. Combining the corresponding NDVI (Supplementary Fig. 3) and erosion potential maps (Supplementary Fig. 4), significant changes in the spatial differences between the land cover and erosion potential during decontamination were also observed.

Response of river SS to land-cover changes

The downstream river SS load (L ; Fig. 4a) exhibited a strong correlation with water discharge (Q) during the monitoring periods (Supplementary Fig. 5 and Supplementary Table 3). Under the range of water discharges from 0.1 to 100 m³ s⁻¹, river SS carrying capacity exhibited a considerable increase from 2013 to 2016 and a slight decrease after decontamination (2017 to 2018). Contrastingly, the range of water discharges was relatively narrow upstream, and a steady decrease in SS loads has been observed since 2015. Although the above result suggests an increase in SS supply during the decontamination stage, the high SS carrying capacity in 2015 is not consistent with the actual decontamination progress. Since decontaminated regions tend to be bare land, sediment loads are prone to increasing during rainstorms due to soil erosion. Governmental decontamination plans showed that over 50% of agricultural land decontamination was planned to be implemented in 2016, implying that the erosion potential of the decontaminated regions should have been higher in 2016, rather than in 2015.

The variations in downstream river SS loads over the 6 years (Supplementary Table 4) exhibited a similar trend to peak river SS load in 2015 ($126.7 \pm 0.3 \text{ Ggyr}^{-1}$). This was an approximately 1,776%, 140% and 215% increase relative to that of 2013, 2016 and 2018, respectively. The historical rainfall records (Fig. 4b) show that the rainfall in September 2015 (551 mm) was more than two-fold greater than that during the same period in 2016 (274 mm), implying that the SS peak may be related to strong runoff. Here we estimate the SS loads at 1-year-flood discharge ($Q = 95 \text{ m}^3 \text{ s}^{-1}$) using established L – Q curves, which allow for the comparison of dynamic variations in SS loads under the same flood conditions. In Fig. 4b, a significant increasing trend during the decontamination period is shown, with a 237.1% increase in 2016 compared with 2013.

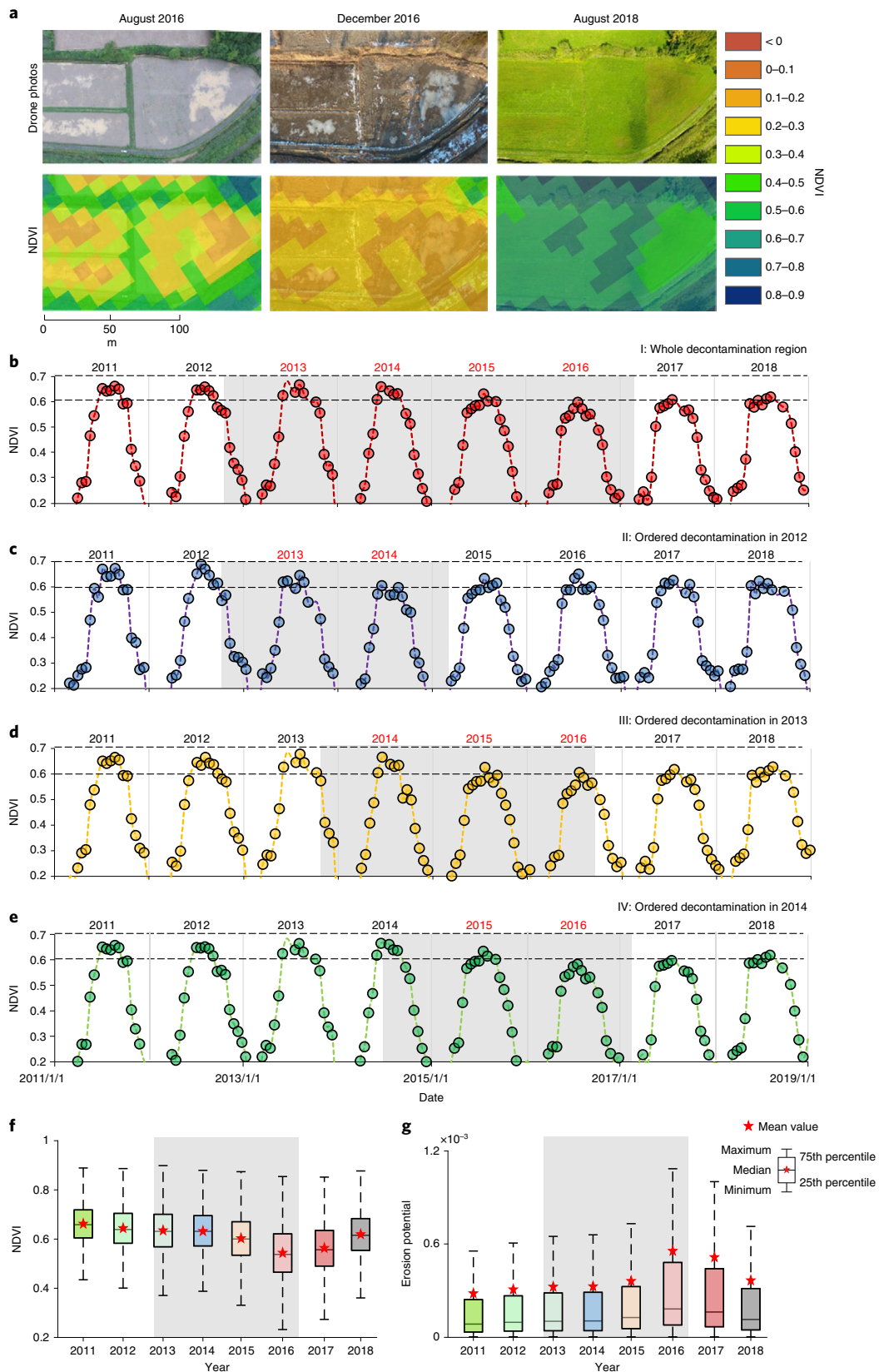


Fig. 3 | Land-cover changes in the decontaminated regions. **a**, Drone photographs and NDVI at Hiso (D3; 37.613° N, 140.711° E) from August 2016, December 2016 and August 2018. **b–e**, NDVI variation curve in all the decontamination regions (**b**) and in the ordered decontamination regions in 2012 (**c**), 2013 (**d**) and 2014 (**e**). Grey shaded backgrounds represent the actual decontamination period. **f, g**, Temporal variations in NDVI (**f**) and erosion potential (**g**; that is, $K \times LS \times C \times P$ in the RUSLE) in August to September during 2011–2018. The dashed black lines in **b–e** are the range of NDVI from 0.6 to 0.7. Each column shows the data distribution. From the top to the bottom, these indicate the maximum, 75th percentile, median, 25th percentile and minimum values.

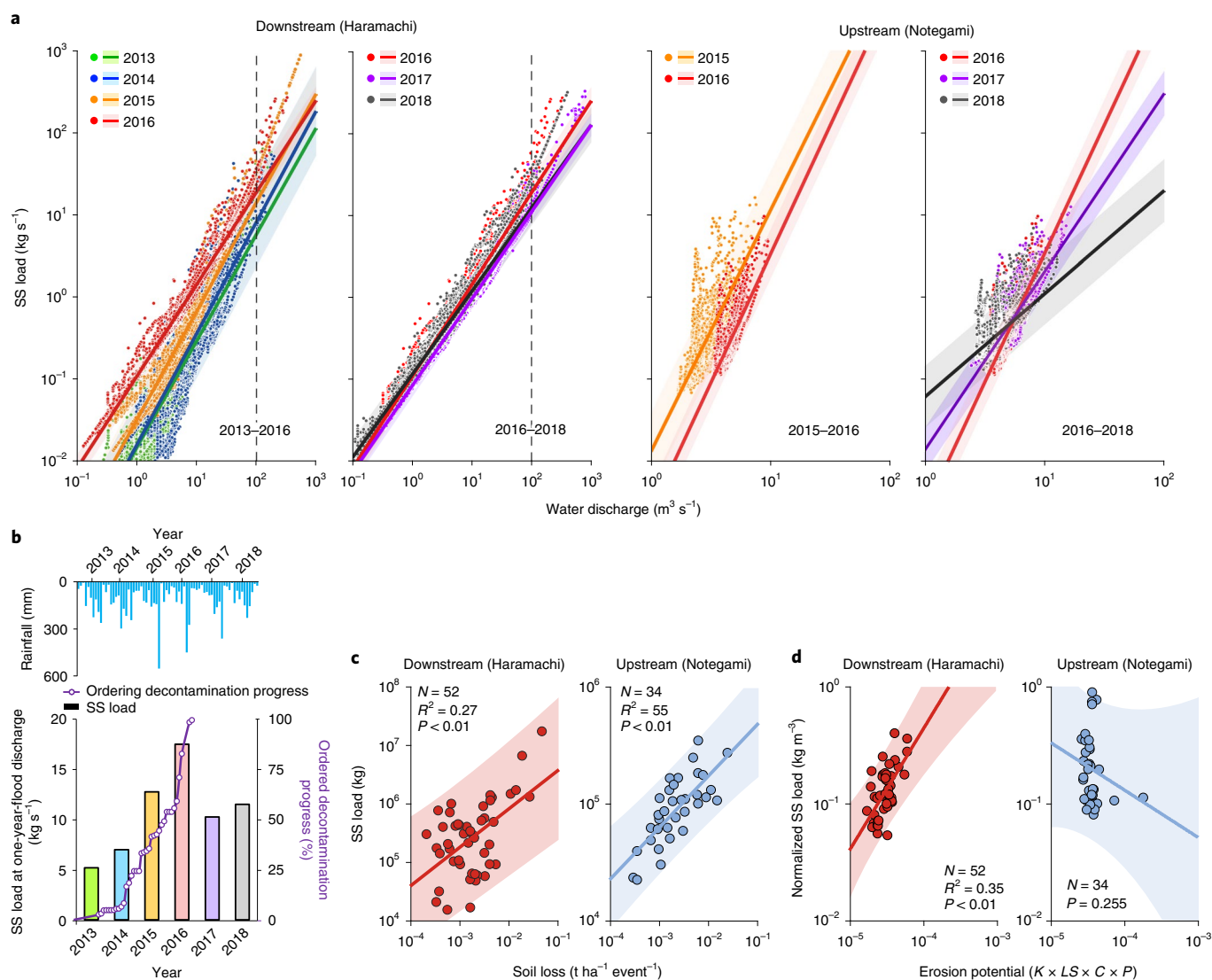


Fig. 4 | Decontamination impact on river SS dynamics. **a**, L–Q curves for Haramachi and Notegami during the study period. The dotted line in the plots for Haramachi represents the one-year-flood discharge. The points are the monitoring data of water discharge (Q) and SS load (L). The solid lines represent the fitting L–Q curves. **b**, Precipitation monitoring data (upper plot), obtained from the official monitoring network of the Japan Meteorological Agency, and the estimated SS loads at one-year-flood discharge with ordered decontamination progress (lower plot) in the Haramachi catchment between 2013 and 2018. **c**, Relationship between the RUSLE-based soil loss (that is, $R \times K \times LS \times C \times P$) from decontaminated regions and river SS load for each rainstorm event (i.e. points) in the downstream (Haramachi) and upstream (Notegami) catchments. **d**, Relationship between the erosion potential (that is, $K \times LS \times C \times P$) and SS load (normalized by water discharge) for each rainstorm event (i.e. points) in the downstream (Haramachi) and upstream (Notegami) catchments. The shaded areas represent the 95% confidential interval of the fitting curves (i.e. solid lines).

After decontamination, the SS loads drastically decreased by approximately 41% from 2016 to 2017, implying changes in sediment yield and transfer patterns due to natural restoration. These results reveal that river SS loads responded closely to land-cover changes during the study period.

To better explore the response of river SS load to land-cover changes, we extracted river monitoring data during each rainfall event and quantitatively linked the river SS to the corresponding soil loss from the decontaminated regions. We found that SS loads during rainstorms were highly correlated with water discharges in both upstream and downstream areas (Supplementary Fig. 6). Comparing similar rainfall events, significantly greater SS concentrations are observed in 2015–2016 than in other years (Supplementary Figs. 7 and 8). Considering that the land-cover changes induced by decontamination were more pronounced in the

summer season, the regression was performed for SS loads between May and October and soil loss during the corresponding period. A more significant correlation was observed (Fig. 4c) between estimated soil loss by RUSLE and SS load upstream ($R^2 = 0.55$, $P < 0.01$, $N = 34$) than downstream ($R^2 = 0.27$, $P < 0.01$, $N = 52$). Eliminating the effect of rainfall and normalizing by discharge (Fig. 4d) results in a more evident relationship between the erosion potential and SS loads downstream ($R^2 = 0.35$, $P < 0.01$, $N = 52$). Overall, these results demonstrate the connection between river SS dynamics and land-cover changes in the decontaminated regions. The short distance between the upstream catchment and decontaminated regions makes soil erosion a critical driver for upstream river SS transport, whereas the downstream river is dependent on long-distance SS transport, making water discharge an important driver for the downstream catchment.

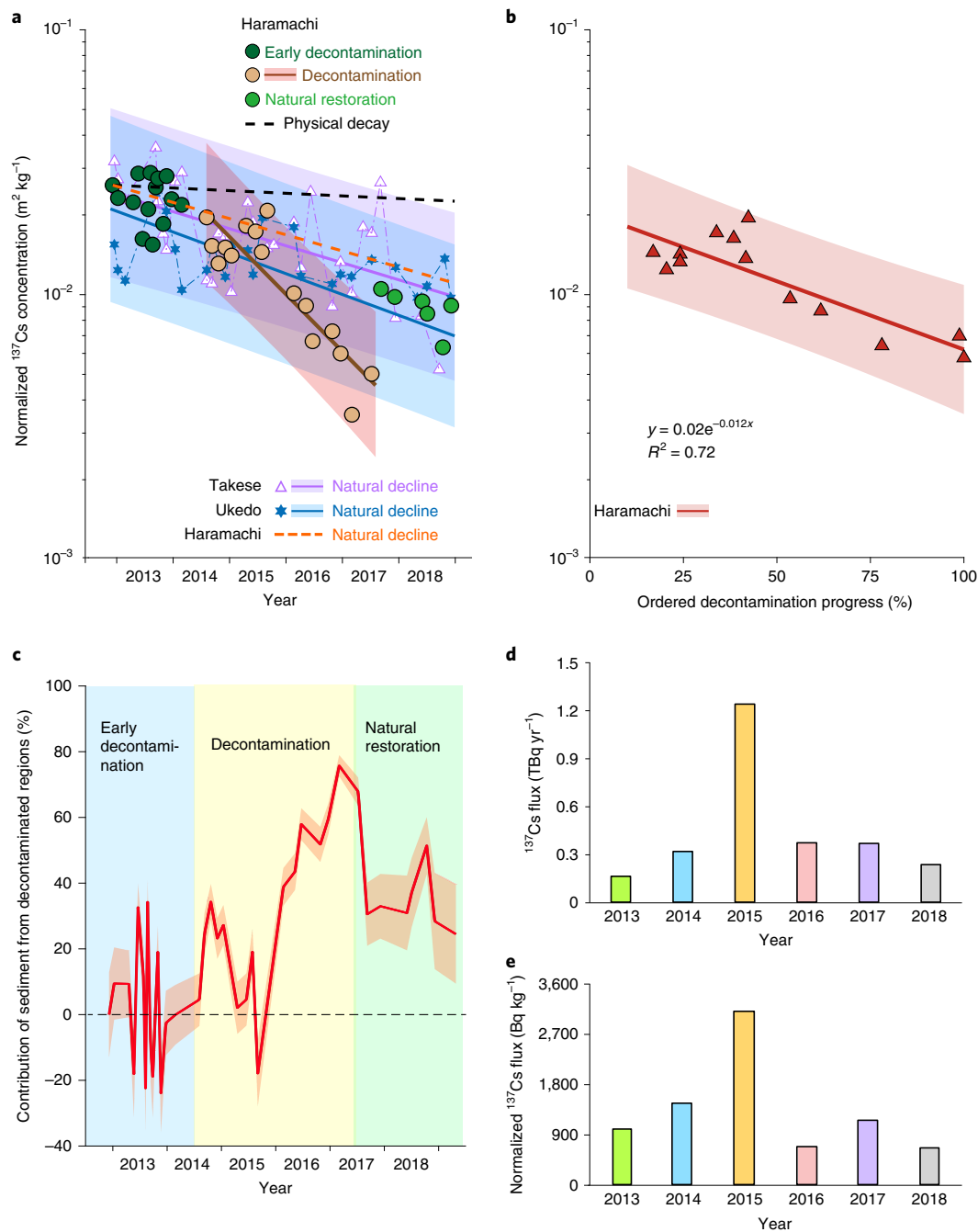


Fig. 5 | Impact of decontamination on downstream particulate ^{137}Cs discharge. **a**, Temporal variations in ^{137}Cs concentrations ($C_m(t)$), normalized by ^{137}Cs catchment inventory) in Haramachi (circles), Takase (purple triangles, $C_m(t) = 0.031e^{-0.149t}$, $P < 0.001$) and Ukedo (blue hexagams, $C_m(t) = 0.029e^{-0.182t}$, $P < 0.001$). The dotted lines represent the ^{137}Cs decline due to physical decay (black) and ^{137}Cs natural decline in the catchment (orange). The solid lines are regression curves of normalized ^{137}Cs concentrations in the three catchments. **b**, Negative correlation between the ^{137}Cs concentration (normalized by ^{137}Cs catchment inventory) in Haramachi and the ordered decontamination progress (triangles), estimated by linear interpolation (red line). **c**, Percentage of SS originating from the decontaminated regions. The contribution was estimated by a mixing source model, and the ^{137}Cs concentration (normalized by ^{137}Cs catchment inventory) in natural decline (mean of temporal variations in ^{137}Cs concentrations in Ukedo and Takase; $C_m(t) = 0.033e^{-0.141t}$) and decontaminated soil were set as two sources. **d**, Temporal variation in annual ^{137}Cs fluxes from downstream of the Niida River (that is, Haramachi) to the ocean. **e**, Temporal variation in the annual ^{137}Cs fluxes in one-year-flood discharge (that is, SS load at $200\text{ m}^3\text{ s}^{-1}$). The shaded areas represent the 95% confidential interval of the fitting curves.

Long-term impact on river SS and ^{137}Cs discharge

From August 2014 to March 2017, the particulate ^{137}Cs concentration in Haramachi exhibited a steep decrease, contrasting remarkably with the limited ^{137}Cs variation observed in the early

decontamination stages (January 2013 to August 2014; Fig. 5a). The effective half-life of the particulate ^{137}Cs (eliminated by the natural attenuation factor) during this decontamination period (1.87 yr) was considerably faster than that of physical decay of

^{137}Cs (30.1 yr), the early decontamination period (16.9 yr) and the surrounding contaminated catchments (mean of 4.92 yr)²⁰. Such a sharp decrease in the ^{137}Cs concentration was also observed at the other three monitoring sites (Supplementary Fig. 9a). Because the ^{137}Cs concentration in decontaminated soil was considerably lower than that in the contaminated soil^{37,42}, these results suggest the contribution of sediment from decontaminated regions to the river system. Moreover, strong negative correlations were observed between measured ^{137}Cs levels and decontamination progress at all monitoring sites (Fig. 5b and Supplementary Fig. 9b), which further supports our interpretation. The observed ^{137}Cs concentration increased by approximately 150% in 2018 compared with that at the end of 2016, which may be caused by the weakened sediment supply from decontaminated regions owing to natural restoration and resulting in a relatively increased contribution of sediments from contaminated forest regions¹³.

Given that the variation in ^{137}Cs concentrations reflects a change in sediment source, the deviations between the measured ^{137}Cs and the natural decrease in ^{137}Cs derived from surrounding contaminated catchments provide a way to quantitatively estimate the contribution of sediment from decontaminated regions (Fig. 5c). In the early decontamination period, our results showed slight variations in the ^{137}Cs concentration (Fig. 5a), which could be attributed to the contribution of sediment from upstream regions with different degrees of contamination. During the main decontamination period, the erosion potential in the summer of 2015 was approximately 22% higher than that in 2014 and the heavy rainfall caused the largest flooding event during the study period (26-year flood). This may result in the sediment from decontaminated regions not being the dominant source for downstream. In 2016, decontamination caused an increase by approximately 59% in the erosion potential compared with 2013, with the contribution percentage steadily increasing over this period to a maximum of $75.7\% \pm 3.2\%$ (value $\pm 95\%$ uncertainty). After decontamination, the decreased contribution of sediment from decontaminated regions and the increased ^{137}Cs concentrations can both be attributed to the reduction of soil loss from upstream due to natural restoration.

The ^{137}Cs discharge from contaminated catchments around the Fukushima region into the Pacific Ocean is another ecological issue of global concern. Our data show that the export flux of particulate ^{137}Cs from the downstream of the Niida river (that is, Haramachi) peaked in 2015 (1.24 TBq yr^{-1} , equalling 0.65% ^{137}Cs loss), which is an approximately 667%, 233% and 429% increase relative to that in 2013, 2016 and 2018, respectively (Fig. 5d). Although such ^{137}Cs loss is negligible compared with the terrestrial inventory, it is approximately 10^5 times greater than that in the pre-Fukushima stage^{43,44}. Accordingly, the dynamic variations in ^{137}Cs discharge from terrestrial environments into the Pacific Ocean, and its drivers, require more attention in the future.

Here we used SS loads at one-year-flood discharge to normalize the ^{137}Cs flux and found its peak occurred in 2015 (Fig. 5e). Additionally, the reduction of the normalized ^{137}Cs flux from 2013 to 2016 ($\sim 32\%$) was similar to natural attenuation in the non-contaminated catchment ($\sim 34\%$) over same period, which may be due to the increased SS load during decontamination offsetting the role of declining ^{137}Cs concentrations in reducing ^{137}Cs emission. During the subsequent natural restoration period, the rapid NDVI increase (Fig. 3f) suggested vegetation recovery in decontaminated regions and a decrease in regional erosion potential (Fig. 3g). This resulted in an approximately 24% decrease in sediment yield from the catchment and an approximately 31% decrease in the contribution of sediment from decontaminated regions (Fig. 5c) from 2016 to 2018. Due to the mutual balance of these effects, there were no significant changes in normalized particulate ^{137}Cs flux in 2018 compared with 2016.

Discussion

Our work highlights the great potential of interdisciplinary analyses for understanding river SS variation and quantifying the contribution of sediment from specific regions. Fukushima decontamination practices, like a controllable validation experiment, justified the reliability of using long-term ^{137}Cs monitoring data for tracing sediment source dynamics due to specific perturbation. Combining the long-term dataset of ^{137}Cs (or other fallout radionuclides) in SS with remote sensing images would provide additional evidence to determine if the changes in the downstream SS transport pattern are linked to the upstream perturbation.

With these interdisciplinary analyses, we systematically reveal how changes in land use in the decontaminated regions significantly influences downstream river SS and ^{137}Cs discharge into the ocean. Indeed, the secondary environmental impacts of surface remediation are being increasingly considered in the broader field concerning remediation of regions contaminated with hazardous materials (for example, heavy metals and organic contaminants)⁴⁵. The concept of environmental sustainability-centred green remediation has also been brought up in many scenarios^{46,47}. The Fukushima decontamination practice provides evidence showing that mechanical remediation can cause persistently excessive SS load downstream, though it also reduced river ^{137}Cs concentrations. Since persistently excessive turbidity in rivers affects not only surrounding residents' water use but also trophic level structure in aquatic environments⁴⁸, the unsustainable downstream impacts caused by upstream decontamination should be highly regarded. The vegetation recovery after land development is highly dependent on local conditions⁴⁹, and the soil used for decontamination and local high rainfall amount in Fukushima promoted rapid vegetation recovery^{11,13}, which shortened the duration of such unsustainable impacts. Therefore, future upstream contaminated lands that await mechanical remediation need to consider the pre-assessment of local natural restoration conditions or the preparation of appropriate revegetation measures in the catchments' regulatory frameworks, which would minimize the impact of long-term decontamination on downstream sustainability.

Methods

Study region. The Niida River Basin (265 km²) is located about 40 km northwest of the damaged FDNPP. The topography of its upstream is almost mountainous and its soil types are mainly cambisols and andosols, while fluvisols are the dominant soil type in the downstream plain⁵⁰. The monitoring data from the Japan Meteorological Agency show that the average rainfall in the Niida River Basin is greater than 1,300 mm, with more than 75% of the rainfall occurring between May and October. According to the third airborne monitoring survey by the Japanese government, the ^{137}Cs inventory in the Niida River Basin was over 700 kBq m^{-2} (ref. 14). Because of particularly high contamination in its upstream watershed (over $1,000 \text{ kBq m}^{-2}$)⁵¹, the government-led decontamination was implemented in the upstream basin from 2013 to 2016 ($\sim 1\%$ of the area was extended to March 2017).

Land-cover observation. We constructed the vector decontamination maps based on the paper maps from the Ministry of the Environment, Japan. The boundaries of the decontaminated regions with different land-use types were first outlined by creating polygons using Google Earth. Subsequently, the projections of these polygons were imported to ArcMap v.10.3 to quantitatively evaluate their area.

During the decontamination (2016) and post-decontamination stages (2018), drone photography was utilized (Fig. 2a, triangle) to compare land-cover changes. A commercially available drone (Phantom 4, DJI product) was employed at 100 m above the ground in Matsuzuka (D1; 37.689° N , 140.720° E), Itoi (D2; 37.663° N , 140.723° E) and Hiso (D3; 37.613° N , 140.711° E) to take photographs.

Quantification of land-cover changes in decontaminated regions. We calculated NDVI within the boundary of the decontaminated regions to quantify the land-cover changes. Through the spectral reflectance dataset in the red (R, nm) and near-infrared (NIR, nm) regions, the NDVI was calculated as⁵²:

$$\text{NDVI} = \frac{\text{NIR} - R}{\text{NIR} + R} \quad (1)$$

The available satellite images from 2011 to 2018 from Sentinel 2 were downloaded from the United States Geological Survey⁵³, while the concurrent MODIS images were derived from the National Aeronautics and Space Administration's Reverb⁵⁴. The wavelength bands and spatiotemporal resolutions of the satellite images used here are summarized in Supplementary Tables 5 and 6.

To confirm the reliability of the newly generated NDVI variation curve, NDVIs for the same date as the Sentinel 2 images were estimated using the interpolation and compared with the Sentinel 2-based NDVI. The linear regression analysis showed that the fitting R^2 was 0.99 ($N=16$, $P<0.01$). We also calculated the NDVI in the decontaminated region based on available satellite images of Landsat 5/7/8 (ref. ⁵⁵) and established a daily NDVI variation curve. The linear regression analysis also showed a high R^2 between two daily NDVI curves ($R^2=0.97$, $N=2868$, $P<0.01$). Therefore, these NDVIs calculated by different satellite images confirmed the reliability of the NDVI variation curve based on ESTARFM.

Estimation of erosion potential in decontaminated regions. To link the land-cover changes in decontaminated regions with the soil erosion dynamics, we defined an erosion potential ($K \times LS \times C \times P$) based on the RUSLE.

The soil loss (A , $\text{t ha}^{-1} \text{yr}^{-1}$) of a specific region can be estimated as⁵⁵:

$$A = R \times K \times LS \times C \times P, \quad (2)$$

where R is the precipitation erosivity factor ($\text{MJ mm ha}^{-1} \text{h}^{-1} \text{yr}^{-1}$), K represents the soil erodibility factor ($\text{t h MJ}^{-1} \text{mm}^{-1}$), L and S are slope length factor (dimensionless) and slope steepness factor (dimensionless), respectively, and C and P are the cover management factor (dimensionless) and support practice factor (dimensionless), respectively. Because these parameters are often set as fixed values, it is difficult to assess the soil loss dynamics during anthropogenic disturbances. To address this problem, we used daily NDVI data to estimate $C \times P$ and then considered these dynamic factors in RUSLE.

Wakiyama et al.⁴⁰ reported a correlation between vegetation cover in Fukushima and the sediment discharges from the standard USLE plot (that is, soil loss, A) that have been normalized by R , K , S and L factors^{40,56}. Therefore, this empirical equation reflects the quantitative relationship between vegetation fractions (VF) and $C \times P$.

To quantify daily $C \times P$ changes in decontaminated regions, we first converted the interpolated daily NDVI into the VF by a semi-empirical equation⁴¹:

$$\text{VF} = 1 - \left(\frac{\text{NDVI} - \text{NDVI}_{\infty}}{\text{NDVI}_s - \text{NDVI}_{\infty}} \right)^{0.6175}, \quad (3)$$

where NDVI_s and NDVI_{∞} represent the NDVI value for land cover corresponding to no plants and 100% green vegetation cover, respectively. Since these values mainly depend on plant species and soil types, we followed previous methods applied to agricultural land and set NDVI_s and NDVI_{∞} as 0.05 and 0.88, respectively⁴¹.

Subsequently, the $C \times P$ was estimated by the empirical equation derived from uncultivated farmlands and grasslands ($R^2=0.47$, $N=145$)⁴⁰:

$$C \times P = 0.083 \times e^{-5.666 \times \text{VF}}. \quad (4)$$

Since the soil type used for decontamination is generally the same, the K factor was set as a constant (0.039; ref. ⁴⁰). For the LS factor, we downloaded a digital elevation model from the Geospatial Information Authority of Japan (spatial resolution: 10 m) to build an LS map using⁵⁵:

$$LS = \left[\frac{Q_a \times M}{22.13} \right]^y \times \left(0.065 + 0.045 \times S_g + 0.0065 \times S_g^2 \right), \quad (5)$$

where Q_a is the flow accumulation grid, S_g represents the grid slope as a percentage, M is the grid size and y is a parameter depended on slope steepness. We here used the y values recommended by a published study, ref. ⁵⁵.

The calculated LS -factor map (Supplementary Fig. 2) showed a relatively consistent LS distribution in space. Based on the ESTARFM-generated satellite images, we compared $C \times P$ and erosion potential ($K \times LS \times C \times P$) and found a significant correlation ($R^2=0.99$, $P<0.01$, $N=174$). Since these results suggest that LS factors in decontaminated regions have a negligible effect on the erosion potential, the mean LS factor and interpolated NDVI based on the daily variation curve (Fig. 3b) were used to estimate the daily erosion potential.

Monitoring of river discharge and turbidity. The water-level gauges (in situ Rugged TROLL100 Data Logger) and a turbidimeter (ANALITE turbidity NEP9530, McVan Instruments) were installed in each monitoring site to continuously recording the water level and turbidity with a temporal resolution of

10 min. As ocean tides may influence the accuracy of water-level monitoring, the Sakekawa site (M4 in Fig. 2) was excluded from the river monitoring programme.

The recorded water level (H , m) was converted to the water discharge (Q , $\text{m}^3 \text{h}^{-1}$) based on the annual H - Q curves for each monitoring site. These curves were calibrated using a synchronous monitoring dataset of 10-min-resolution water level and discharge provided by the Fukushima prefecture's official monitoring network⁵⁷. Because of occasional damage to the water-level gauge at the Haramachi site, the available monitoring data with a temporal resolution of 10 min recorded by the Fukushima prefecture's official monitoring network⁵⁷ were used to fill the gaps. The percentages of filling data from official monitoring network were all less than 34% except for 2015 (56.6%). Although similar situations occurred in Notegami, we were unable to fill in gaps with other data due to the lack of a concurrent monitoring network.

The hourly SS concentration (C_{ss} , g m^{-3}) at each monitoring site was calculated from the measured turbidity (T , mV) using a calibrated curve²⁰. As the turbidimeter was susceptible to the moss and debris flowing in the river, the dataset was verified with an automated check by HEC-DSSVue (The U.S. Army Corps of Engineers' Hydrologic Engineering Center Data Storage System) before transforming the data.

The SS load was estimated as the product of the corresponding datasets of discharge and SS concentration, after which we can obtain the annual SS load (L , ton yr^{-1}) by taking the sum:

$$L = \sum (Q \times C_{ss}). \quad (6)$$

We estimated values for gaps including missing and abnormal data through a linear model established by 10-min-resolution monitoring data at the same site. The reliability of the gap-filling strategies used in this study has been documented by Taniguchi et al.^{19,20} These procedures vastly enhance the possibility of reconstructing the complete dataset. In this study, only the error in converting from water discharge to SS load was considered in the uncertainty assessment, and all estimates were within 0.5% (95% confidential interval) in this case. To reduce the uncertainty of L - Q fitting, the 10-min monitoring dataset (discharge and SS load) was transformed to a 1-hour dataset.

Considering the river SS is often transported by discharge, we used downstream L - Q curves to estimate river SS loads at 1-year-flood discharge ($Q=95 \text{ m}^3 \text{ s}^{-1}$), which eliminates the influence caused by different annual water discharges. The 1-year-flood discharge was calculated from the daily maximum discharge data from 1 January 2013 to 30 September 2020 at the Haramachi site.

To compare river SS dynamics during rainfall events, we here defined a rainfall event as the increase in water discharge exceeding 1.4 and 1.6 times the baseflow before precipitation for the upstream and downstream catchments, respectively. As a result, a total of 64 and 72 rainfall events from the Notegami and Haramachi sites were identified.

To study the dynamic relationship between soil loss from decontaminated regions and river SS load, we estimated eroded soil amount during each rainstorm using RUSLE. Specifically, the NDVI during a specific rainfall was determined by interpolation. Subsequently, the corresponding $C \times P$ can be estimated using equations (3) and (4). With the mean values of the K and LS factors, the erosion potential can then be calculated. Finally, precipitation erosivity factor (Supplementary Table 7) for each rainfall event can be calculated as⁵⁸:

$$R = \frac{1}{n} \sum_{j=1}^n \sum_{k=1}^{m_j} (EI_{30})_k, \quad (7)$$

where n is the number of years used, m_j is the number of precipitation events in each given year j and E and I_{30} represent each event's kinetic energy (MJ) and maximum 30 min precipitation intensity (mm h^{-1}), respectively, for each event k . The event's erosivity, EI_{30} , can be calculated as⁵⁸:

$$EI_{30} = \left(\sum_{r=1}^0 e_r v_r \right) I_{30}, \quad (8)$$

where e_r denotes the unit rainfall energy ($\text{MJ ha}^{-1} \text{mm}^{-1}$) and v_r provides the rainfall volume during a set period (r) (mm). For this calculation, the criterion for the identification of a precipitation event is consistent with previous work, that is, the cumulative rainfall of an event is greater than 12.7 mm (ref. ⁵⁸). If another rainfall event occurs within 6 h of the end of a rainfall event, they are counted as one event. Therefore, the unit rainfall energy (e_r) can be derived for each time interval based on rainfall intensity (i_r , mm h^{-1})⁵⁸:

$$e_r = 0.29 \left[1 - 0.72e^{(-0.05 \times i_r)} \right]. \quad (9)$$

The calculation's required parameters were derived from the historical precipitation record from the Japan Meteorological Agency⁵⁹. For the Notegami catchment, the precipitation monitoring data were derived from Iitate. For the Haramachi catchment, the precipitation was obtained from three adjacent monitoring sites (that is, Haramachi, Iitate and Tsushima) with the specific weights

of 0.143, 0.545 and 0.312, respectively. These weights were determined by the Voronoi diagram method in a Geographic Information System⁶⁰.

River monitoring of particulate ¹³⁷Cs. At each monitoring site, the suspended sediment sampler proposed by Phillips et al.⁶¹ was installed at 20–30 cm above the riverbed for the time-integrated sampling of river suspended sediment. The reliability of this sampler has been widely proven in past studies^{19,20}. After sampling, the trapped turbid water and SS samples were transferred into a clean polyethylene container and stored until laboratory analysis.

The SS samples were separated from the collected water mixture via natural precipitation and physical filtration, dried at 105 °C for 24 h and subsequently packed into a plastic container. The activities of ¹³⁷Cs in the SS samples (C_s , Bq kg⁻¹) were determined via the measurement system, which consists of a high-purity germanium γ -ray spectrometer (GCW2022S, Canberra–Eurisyss, Meriden) coupled to an amplifier (PSC822, Canberra, Meriden) and multichannel analyser (DSA1000, Canberra, Meriden). The measurement system was calibrated with the standard soil sample from the International Atomic Energy Agency. Under the 662 keV energy channel, each measurement batch would take approximately 1–24 h to make the analytical precision of the measurements within 10% (95% confidential interval). All measured ¹³⁷Cs concentrations were decay-corrected to their sampling date. Moreover, the results obtained in this study were also normalized by their initial average ¹³⁷Cs inventory in the catchment (D , Bq m⁻²) to eliminate the effect caused by spatial differences.

As ¹³⁷Cs concentration in the sediment sample depends on particle size^{19,20}, we conducted a particle size correction for all measured data in Takase, Ukedo and Haramachi to eliminate this effect. The particle size distributions for dried SS samples were analysed using the laser diffraction particle size analyser (SALD-3100, Shimadzu Co., Ltd.). With the parameterized particle size distributions, the particle size correction coefficient (P_c) can be calculated by¹⁹:

$$P_c = \left(\frac{S_s}{S_r} \right)^v, \quad (10)$$

where S_s and S_r represent the reference and collected samples' specific surface areas (m² g⁻¹). The exponent coefficient, v , is a fitting parameter associated with chemical and mineral compositions. In this study, the same parameters measured in the Abukuma River, the major river in the Fukushima area, were applied for S_r (0.202 m² g⁻¹) and v (0.65). The specific surface area for collected SS samples was estimated by the following equation under a spherical approximation⁴⁰:

$$S_s = \sum \left(6 \times \rho^{-1} \times d_i^{-1} \times p_i^{-1} \right), \quad (11)$$

where ρ is the particle density and d_i and p_i denote the ratio and diameter of the particle size fraction for particle i . Therefore, the ¹³⁷Cs concentration corrected for particle size can be obtained by dividing the measured ¹³⁷Cs concentration by P_c .

Considering that the decrease in particulate ¹³⁷Cs concentration in a catchment was also affected by natural attenuation, there is a need to eliminate this effect from the declining trend of our observed ¹³⁷Cs dataset to highlight the impacts of decontamination. The Ukedo and Takase are rivers surrounding the Niida River with similar contaminated situations. Our long-term ¹³⁷Cs monitoring data from downstream of these two catchments showed that their ¹³⁷Cs decline trends were relatively steady. Although there is a dam reservoir upstream of Ukedo, the ¹³⁷Cs concentration observed both upstream and downstream showed a similar declining trend⁶². Therefore, the above evidence suggests that natural attenuation was the dominant factor controlling the ¹³⁷Cs decrease in these two rivers. Here we assumed that the natural attenuation trend of ¹³⁷Cs in the surrounding catchments (Ukedo and Takase) with little effect by decontamination was similar to that of the Haramachi catchment. Thus, we fitted their time change curves of ¹³⁷Cs concentration (normalized by average ¹³⁷Cs inventory of the corresponding catchment) using an exponential model. We then estimated the ¹³⁷Cs concentration at the same sampling time as Haramachi in the two catchments by using the fitting models. Finally, we calculated the mean value of the two datasets and recalculated the effective half-life ($T_{\text{eff}} = \ln(2)/\lambda$; λ is the fitting exponential term) of the natural attenuation by the exponential model.

The ¹³⁷Cs flux (L_{Cs} , Bq) for each monitoring site was estimated by the product of the SS flux and the ¹³⁷Cs concentration in the suspended sediment sample. We then took the sum over that year:

$$L_{Cs} = \sum (Q \times C_{ss} \times C). \quad (12)$$

According to the law of error propagation, we considered the error from SS load and ¹³⁷Cs measurement in the combined uncertainty assessment for ¹³⁷Cs fluxes and found their values are all within 1.1% (95% confidential interval).

Using ¹³⁷Cs as a tracer in estimating SS source contribution. Although ¹³⁷Cs has been widely used in tracing sediment source, the spatial variability of the ¹³⁷Cs deposition inventory in the Fukushima catchment hinders the estimation of the source contribution from a specific region. However, for the decontaminated catchments, as the ¹³⁷Cs concentration in decontaminated soil was much lower

than that in contaminated regions (for example, forested regions and the riverbank)^{11,13,63}, the fluctuations in the particulate ¹³⁷Cs concentration can help to identify the sediment from the decontamination regions. Specifically, we assumed that the particulate ¹³⁷Cs concentrations in surrounding contaminated watersheds (that is, having similar land-use composition) follow a similar decline trend driven by natural reasons, while the decontamination-induced land-cover changes cause other sediment sources to mix with the original river SS and thus result in a deviation in observed ¹³⁷Cs concentrations from this natural trend. Therefore, the relative contribution (RC) of the specific sediment source can be expressed as:

$$RC = \frac{(C_m - C_n)}{(C_s - C_n)}, \quad (13)$$

where the C_m is the measured ¹³⁷Cs concentration and C_s and C_n represent the ¹³⁷Cs concentration in a specific sediment source and the naturally varied ¹³⁷Cs concentration at the same time as the measured ¹³⁷Cs. For data comparability, all ¹³⁷Cs concentrations presented here were corrected by their particle size and ¹³⁷Cs inventory. We also excluded the samples with collection weights below 0.5 g from the calculations due to their high uncertainty in P_c measurement.

In this study, the specific sediment source is the decontaminated soil in the Niida River Basin where the ¹³⁷Cs concentration was approximately 53.99 ± 40.90 Bq kg⁻¹ (refs. 37,42; mean ± standard deviation, $N=8$). The natural decline of the ¹³⁷Cs concentration (that is, λ) was established using temporal variation in ¹³⁷Cs data originating from the Ukedo and Takase rivers, which were scarcely influenced by decontamination. The first measured ¹³⁷Cs data in Haramachi were set as the starting point of its natural decline curve. The total uncertainty for the contribution percentage of SS from the decontaminated regions was calculated by the propagation of error from each part with the uncertainties originating from the measured ¹³⁷Cs concentration, ¹³⁷Cs concentration in a specific source and the natural ¹³⁷Cs concentration. For the uncertainty in the ¹³⁷Cs concentration in decontaminated soil (C_s), we set the standard deviation as its error source, while the natural ¹³⁷Cs concentrations were calculated by the propagation of the 95% confidential interval of the fitting curves.

Reporting summary. Further information on research design is available in the Nature Research Reporting Summary linked to this article.

Data availability

Ordered decontamination process data are available from http://josen.env.go.jp/plaza/info/weekly/weekly_190607.html. Particulate ¹³⁷Cs monitoring data in Haramachi, Takase and Ukedo during 2012–2017 are available from: <https://doi.org/10.34355/Fukushima.Pref.CEC.00014>, <https://doi.org/10.34355/CRIED.U.Tsukuba.00020> and <https://doi.org/10.34355/Fukushima.Pref.CEC.00021>. The rest of data presented in this study are available from the corresponding author upon request.

Received: 18 November 2021; Accepted: 2 June 2022;

Published online: 14 July 2022

References

1. Anspaugh, L. R., Catlin, R. J. & Goldman, M. The global impact of the Chernobyl reactor accident. *Science* **242**, 1513–1519 (1988).
2. Ten Hoeve, J. E. & Jacobson, M. Z. Worldwide health effects of the Fukushima Daiichi nuclear accident. *Energy Environ. Sci.* **5**, 8743–8757 (2012).
3. Shagina, N. B. et al. Reconstruction of the contamination of the Techa River in 1949–1951 as a result of releases from the “MAYAK” Production Association. *Radiat. Environ. Biophys.* **51**, 349–366 (2012).
4. Jones, S. Windscale and Kyshtym: a double anniversary. *J. Environ. Radioact.* **99**, 1–6 (2008).
5. Beresford, N. A. et al. Thirty years after the Chernobyl accident: what lessons have we learnt? *J. Environ. Radioact.* **157**, 77–89 (2016).
6. Steinhäuser, G., Brandl, A. & Johnson, T. E. Comparison of the Chernobyl and Fukushima nuclear accidents: a review of the environmental impacts. *Sci. Total Environ.* **470–471**, 800–817 (2014).
7. Fesenko, S. V. et al. An extended critical review of twenty years of countermeasures used in agriculture after the Chernobyl accident. *Sci. Total Environ.* **383**, 1–24 (2007).
8. Poston, T. M., Peterson, R. E. & Cooper, A. T. Past radioactive particle contamination in the Columbia River at the Hanford site, USA. *J. Radiol. Prot.* **27**, A45 (2007).
9. Voitkevich, O., Nasvit, O., Los'y, I. & Berkovsky, V. Present thoughts on the aquatic countermeasures applied to regions of the Dnieper River catchment contaminated by the 1986 Chernobyl accident. *Stud. Environ. Sci.* **68**, 75–85 (1997).
10. Ramzaev, V., Barkovsky, A., Mishine, A., Andersson, K. G. & Well-being, H. Decontamination tests in the recreational areas affected by the Chernobyl accident: efficiency of decontamination and long-term stability of the effects. *J. Soc. Remediat. Radioact. Contam. Environ.* **1**, 93–107 (2013).

11. Evrard, O., Patrick Lacey, J. & Nakao, A. Effectiveness of landscape decontamination following the Fukushima nuclear accident: a review. *Soil* **5**, 333–350 (2019).
12. Kinase, T. et al. The seasonal variations of atmospheric $^{134,137}\text{Cs}$ activity and possible host particles for their resuspension in the contaminated areas of Tsushima and Yamakiya, Fukushima, Japan. *Prog. Earth Planet. Sci.* **5**, 12 (2018).
13. Onda, Y. et al. Radionuclides from the Fukushima Daiichi Nuclear Power Plant in terrestrial systems. *Nat. Rev. Earth Environ.* **1**, 644–660 (2020).
14. Kato, H., Onda, Y., Gao, X., Sanada, Y. & Saito, K. Reconstruction of a Fukushima accident-derived radiocesium fallout map for environmental transfer studies. *J. Environ. Radioact.* **210**, 105996 (2019).
15. *Remediation of Contaminated Areas in the Aftermath of the Accident at the Fukushima Daiichi Nuclear Power Station. Overview, Analysis and Lessons Learned. Part 1. A Report on the “Decontamination Pilot Project”* (Japan Atomic Energy Agency, 2015); <https://jopss.jaea.go.jp/pdfdata/JAEA-Review-2014-051.pdf>
16. *Decontamination Guidelines* 2nd edn (Ministry of the Environment, 2013); http://josen.env.go.jp/en/%0Aframework/pdf/decontamination_guidelines_2nd.pdf
17. Iwagami, S. et al. Temporal changes in dissolved ^{137}Cs concentrations in groundwater and stream water in Fukushima after the Fukushima Dai-ichi Nuclear Power Plant accident. *J. Environ. Radioact.* **166**, 458–465 (2017).
18. Aoyama, M., Tsumune, D., Inomata, Y. & Tateda, Y. Mass balance and latest fluxes of radiocesium derived from the Fukushima accident in the western North Pacific Ocean and coastal regions of Japan. *J. Environ. Radioact.* **217**, 106206 (2020).
19. Taniguchi, K. et al. Transport and redistribution of radiocesium in Fukushima fallout through rivers. *Environ. Sci. Technol.* **53**, 12339–12347 (2019).
20. Taniguchi, K. et al. Dataset on the 6-year radiocesium transport in rivers near Fukushima Daiichi Nuclear Power Plant. *Sci. Data* **7**, 433 (2020).
21. Walling, D. E. Human impact on land–ocean sediment transfer by the world’s rivers. *Geomorphology* **79**, 192–216 (2006).
22. Borrelli, P. et al. An assessment of the global impact of 21st century land use change on soil erosion. *Nat. Commun.* **8**, 2013 (2017).
23. Piao, S. et al. Changes in climate and land use have a larger direct impact than rising CO_2 on global river runoff trends. *Proc. Natl Acad. Sci. USA* **104**, 15242–15247 (2007).
24. Jung, M., Rowhani, P. & Scharlemann, J. P. W. Impacts of past abrupt land change on local biodiversity globally. *Nat. Commun.* **10**, 5474 (2019).
25. Borrelli, P. et al. Land use and climate change impacts on global soil erosion by water (2015–2070). *Proc. Natl Acad. Sci. USA* **117**, 21994–22001 (2020).
26. Overeem, I. et al. Substantial export of suspended sediment to the global oceans from glacial erosion in Greenland. *Nat. Geosci.* **10**, 859–863 (2017).
27. Giam, X., Olden, J. D. & Simberloff, D. Impact of coal mining on stream biodiversity in the US and its regulatory implications. *Nat. Sustain.* **1**, 176–183 (2018).
28. Hackney, C. R. et al. River bank instability from unsustainable sand mining in the lower Mekong River. *Nat. Sustain.* **3**, 217–225 (2020).
29. Wang, S. et al. Reduced sediment transport in the Yellow River due to anthropogenic changes. *Nat. Geosci.* **9**, 38–41 (2016).
30. *Environmental Remediation* (Ministry of the Environment, Government of Japan, 2021); <http://josen.env.go.jp/en/decontamination/>
31. Niizato, T. & Watanabe, T. ^{137}Cs outflow from forest floor adjacent to a residential area: comparison of decontaminated and non-decontaminated forest floor. *Glob. Environ. Res.* **24**, 129–136 (2021); http://www.airies.or.jp/ebook/Global_Environmental_Research_Vol.24No.2.pdf
32. Sakuma, K. et al. Evaluation of sediment and ^{137}Cs redistribution in the Oginosawa River catchment near the Fukushima Dai-ichi Nuclear Power Plant using integrated watershed modeling. *J. Environ. Radioact.* **182**, 44–51 (2018).
33. Iwagami, S. et al. Six-year monitoring study of ^{137}Cs discharge from headwater catchments after the Fukushima Dai-ichi Nuclear Power Plant accident. *J. Environ. Radioact.* **210**, 106001 (2019).
34. Ochiai, S. et al. Effects of radiocesium inventory on ^{137}Cs concentrations in river waters of Fukushima, Japan, under base-flow conditions. *J. Environ. Radioact.* **144**, 86–95 (2015).
35. Evrard, O. et al. Impact of the 2019 typhoons on sediment source contributions and radiocesium concentrations in rivers draining the Fukushima radioactive plume, Japan. *Collect. C. R. Geosci.* **352**, 199–211 (2020).
36. Evrard, O. et al. Quantifying the dilution of the radiocesium contamination in Fukushima coastal river sediment (2011–2015). *Sci. Rep.* **6**, 34828 (2016).
37. Evrard, O. et al. Radionuclide contamination in flood sediment deposits in the coastal rivers draining the main radioactive pollution plume of Fukushima Prefecture, Japan (2011–2020). *Earth Syst. Sci. Data* **13**, 2555–2560 (2021).
38. Chu, H., Venevsky, S., Wu, C. & Wang, M. NDVI-based vegetation dynamics and its response to climate changes at Amur-Heilongjiang River Basin from 1982 to 2015. *Sci. Total Environ.* **650**, 2051–2062 (2019).
39. Zhu, X., Chen, J., Gao, F., Chen, X. & Masek, J. G. An enhanced spatial and temporal adaptive reflectance fusion model for complex heterogeneous regions. *Remote Sens. Environ.* **114**, 2610–2623 (2010).
40. Wakiyama, Y., Onda, Y., Yoshimura, K., Igarashi, Y. & Kato, H. Land use types control solid wash-off rate and entrainment coefficient of Fukushima-derived ^{137}Cs , and their time dependence. *J. Environ. Radioact.* **210**, 105990 (2019).
41. Gao, L. et al. Remote sensing algorithms for estimation of fractional vegetation cover using pure vegetation index values: a review. *ISPRS J. Photogramm. Remote Sens.* **159**, 364–377 (2020).
42. Nemoto, T. & Matsuki, N. *Soil Stratification Survey on Farmland Soil after Decontamination in Iitate Village* (in Japanese) (Fukushima Agricultural Technology Centre, 2015).
43. Wakiyama, Y., Onda, Y., Mizugaki, S., Asai, H. & Hiramatsu, S. Soil erosion rates on forested mountain hillslopes estimated using ^{137}Cs and $^{210}\text{Pb}_{\text{ex}}$. *Geoderma* **159**, 39–52 (2010).
44. Fukuyama, T., Takenaka, C. & Onda, Y. ^{137}Cs loss via soil erosion from a mountainous headwater catchment in central Japan. *Sci. Total Environ.* **350**, 238–247 (2005).
45. Hou, D., Gu, Q., Ma, F. & O’Connell, S. Life cycle assessment comparison of thermal desorption and stabilization/solidification of mercury contaminated soil on agricultural land. *J. Clean. Prod.* **139**, 949–956 (2016).
46. Ding, D., Song, X., Wei, C. & LaChance, J. A review on the sustainability of thermal treatment for contaminated soils. *Environ. Pollut.* **253**, 449–463 (2019).
47. Hou, D. & Al-Tabbaa, A. Sustainability: a new imperative in contaminated land remediation. *Environ. Sci. Policy* **39**, 25–34 (2014).
48. Kemp, P., Sear, D., Collins, A., Naden, P. & Jones, I. The impacts of fine sediment on riverine fish. *Hydrol. Process.* **25**, 1800–1821 (2011).
49. Copeland, S. M., Munson, S. M., Bradford, J. B. & Butterfield, B. J. Influence of climate, post-treatment weather extremes, and soil factors on vegetation recovery after restoration treatments in the southwestern US. *Appl. Veg. Sci.* **22**, 85–95 (2019).
50. Lepage, H. et al. Investigating the source of radiocesium contaminated sediment in two Fukushima coastal catchments with sediment tracing techniques. *Anthropocene* **13**, 57–68 (2016).
51. Delmas, M., Garcia-Sanchez, L., Nicoulaud-Gouin, V. & Onda, Y. Improving transfer functions to describe radiocesium wash-off fluxes for the Niida River by a Bayesian approach. *J. Environ. Radioact.* **167**, 100–109 (2017).
52. E. I. Jazouli, A. et al. Soil erosion modeled with USLE, GIS, and remote sensing: a case study of Ikkour watershed in Middle Atlas (Morocco). *Geosci. Lett.* **4**, 25 (2017).
53. *EarthExplorer* (USGS, accessed November 2021); <https://earthexplorer.usgs.gov/>
54. *EARTHDATA SEARCH* (NASA, accessed November 2021); <https://search.earthdata.nasa.gov/search?lat=-0.0703125>
55. Ganasri, B. P. & Ramesh, H. Assessment of soil erosion by RUSLE model using remote sensing and GIS—a case study of Nethravathi Basin. *Geosci. Front.* **7**, 953–961 (2016).
56. Yoshimura, K., Onda, Y. & Kato, H. Evaluation of radiocaesium wash-off by soil erosion from various land uses using USLE plots. *J. Environ. Radioact.* **139**, 362–369 (2015).
57. *River Monitoring Network in Fukushima Prefecture* (Fukushima Prefecture, accessed November 2021); <http://kaseninf.pref.fukushima.jp/gis/>
58. Panagos, P. et al. Rainfall erosivity in Europe. *Sci. Total Environ.* **511**, 801–814 (2015).
59. *Historical Meteorological Record* (Japan Meteorological Agency, accessed November 2021); <https://www.jma.go.jp/jma/indexe.html>
60. Di, Z. W. et al. Centroidal Voronoi tessellation based methods for optimal rain gauge location prediction. *J. Hydrol.* **584**, 124651 (2020).
61. Phillips, J. M., Russell, M. A. & Walling, D. E. Time-integrated sampling of fluvial suspended sediment: a simple methodology for small catchments. *Hydrol. Process.* **14**, 2589–2602 (2000).
62. Funaki, H., Sakuma, K., Nakanishi, T., Yoshimura, K. & Katengeza, E. W. Reservoir sediments as a long-term source of dissolved radiocaesium in water system; a mass balance case study of an artificial reservoir in Fukushima, Japan. *Sci. Total Environ.* **743**, 140668 (2020).
63. Lacey, J. P., Huon, S., Onda, Y., Vaury, V. & Evrard, O. Do forests represent a long-term source of contaminated particulate matter in the Fukushima Prefecture? *J. Environ. Manage.* **183**, 742–753 (2016).

Acknowledgements

We appreciate B. Matsushita for his valuable suggestions on satellite image processing and NDVI calculation, J. Chen for sharing the code for ESTARFM, J. Takahashi for sharing ^{137}Cs in decontaminated soil data, H. Kato for his suggestions on presenting the results, S. Fujiwara for his assistance on calculating the precipitation erosivity factor, Y. Yamanaka and T. Kubo for their work on decontamination map development, field investigation and preliminary data analysis and Y. He and F. Yoshimura for their constructive suggestions on improving figure quality. We also acknowledge funding

support from the commissioned study from the Ministry of Education, Culture, Sports, Science and Technology (MEXT) FY2011–2012, Nuclear Regulation Authority FY2013–2014, Japan Atomic Energy Agency-funded FY2015–2021, Grant-in-Aid for Scientific Research on Innovative Areas grant number 24110005, Grant-in-Aid for Scientific Research (A) 22H00556, Agence Nationale de la Recherche ANR-11-RSNR-0002 and the Japan Science and Technology Agency as part of the Belmont Forum.

Author contributions

B.F. and Y.O. conceived the study; B.F. performed the data evaluation and all analyses, interpreted the data, wrote the manuscript and prepared all figures and tables in close discussion with Y.O.; Y.O. provided funding support for the field monitoring and all needed resources; K.T. and Y.Z. outlined the boundary of the decontamination regions and implemented the drone observations of the sites; and Y.W. and K.T. performed the field river monitoring and determined the particulate ^{137}Cs concentration. B.F., A.H. and Y.Z. prepared all satellite images, ran the NDVI calculation and processed ESTARFM. All listed authors contributed to the editing of the manuscript and approved the final version.

Competing interests

The authors declare no competing interests.

Additional information

Supplementary information The online version contains supplementary material available at <https://doi.org/10.1038/s41893-022-00924-6>.

Correspondence and requests for materials should be addressed to Yuichi Onda.

Peer review information *Nature Sustainability* thanks Kazuyuki Sakuma, Qina Yan and the other, anonymous, reviewer(s) for their contribution to the peer review of this work.

Reprints and permissions information is available at www.nature.com/reprints.

Publisher's note Springer Nature remains neutral with regard to jurisdictional claims in published maps and institutional affiliations.



Open Access This article is licensed under a Creative Commons Attribution 4.0 International License, which permits use, sharing, adaptation, distribution and reproduction in any medium or format, as long as you give appropriate credit to the original author(s) and the source, provide a link to the Creative Commons license, and indicate if changes were made. The images or other third party material in this article are included in the article's Creative Commons license, unless indicated otherwise in a credit line to the material. If material is not included in the article's Creative Commons license and your intended use is not permitted by statutory regulation or exceeds the permitted use, you will need to obtain permission directly from the copyright holder. To view a copy of this license, visit <http://creativecommons.org/licenses/by/4.0/>.

© The Author(s) 2022, corrected publication 2022

Reporting Summary

Nature Research wishes to improve the reproducibility of the work that we publish. This form provides structure for consistency and transparency in reporting. For further information on Nature Research policies, see our [Editorial Policies](#) and the [Editorial Policy Checklist](#).

Statistics

For all statistical analyses, confirm that the following items are present in the figure legend, table legend, main text, or Methods section.

n/a Confirmed

- The exact sample size (n) for each experimental group/condition, given as a discrete number and unit of measurement
- A statement on whether measurements were taken from distinct samples or whether the same sample was measured repeatedly
- The statistical test(s) used AND whether they are one- or two-sided
Only common tests should be described solely by name; describe more complex techniques in the Methods section.
- A description of all covariates tested
- A description of any assumptions or corrections, such as tests of normality and adjustment for multiple comparisons
- A full description of the statistical parameters including central tendency (e.g. means) or other basic estimates (e.g. regression coefficient) AND variation (e.g. standard deviation) or associated estimates of uncertainty (e.g. confidence intervals)
- For null hypothesis testing, the test statistic (e.g. F , t , r) with confidence intervals, effect sizes, degrees of freedom and P value noted
Give P values as exact values whenever suitable.
- For Bayesian analysis, information on the choice of priors and Markov chain Monte Carlo settings
- For hierarchical and complex designs, identification of the appropriate level for tests and full reporting of outcomes
- Estimates of effect sizes (e.g. Cohen's d , Pearson's r), indicating how they were calculated

Our web collection on [statistics for biologists](#) contains articles on many of the points above.

Software and code

Policy information about [availability of computer code](#)

Data collection Here, we used Tera Term (version: 4.105) and Omni7 (version 7.2.111) for collecting the turbidity and water level data in the monitored river, respectively.

Data analysis Here, we used ArcGIS (version: 10.8.1; Esri Inc.) and QGIS (version: 3.16.7; QGIS Development Team) for processing satellite data and making map. We used the open source code provided by Prof. J. Chen (<http://www.chen-lab.club/>) for MODIS-SENTINEL 2 transfers in ENVI (version: 5.3.1; Exelis Inc.) and data pretreatment was completed in IDL (version: 8.5, Exelis Visual Information Solutions, Inc.). We corrected abnormal turbidity in HEC-DSSVue (version: 3.2.3 Beta; US Army Corps of Engineers) and analyzed particulate Cs-137 concentration in Genie 2000 software (CANBERRA Industries Inc.). We process the data and statistical analysis in IBM SPSS statistic (version: 22.0; IBM corp.), MATLAB (version: R2020b; The MathWorks, Inc.), and Microsoft Office (version: 2019; Microsoft corp.)

For manuscripts utilizing custom algorithms or software that are central to the research but not yet described in published literature, software must be made available to editors and reviewers. We strongly encourage code deposition in a community repository (e.g. GitHub). See the Nature Research [guidelines for submitting code & software](#) for further information.

Data

Policy information about [availability of data](#)

All manuscripts must include a [data availability statement](#). This statement should provide the following information, where applicable:

- Accession codes, unique identifiers, or web links for publicly available datasets
- A list of figures that have associated raw data
- A description of any restrictions on data availability

Ordering decontamination process data are available from http://josen.env.go.jp/plaza/info/weekly/weekly_190607.html; Particulate 137Cs monitoring data in

Field-specific reporting

Please select the one below that is the best fit for your research. If you are not sure, read the appropriate sections before making your selection.

Life sciences Behavioural & social sciences Ecological, evolutionary & environmental sciences

For a reference copy of the document with all sections, see [nature.com/documents/nr-reporting-summary-flat.pdf](https://www.nature.com/documents/nr-reporting-summary-flat.pdf)

Ecological, evolutionary & environmental sciences study design

All studies must disclose on these points even when the disclosure is negative.

Study description

Severe soil Cs- contamination caused by Fukushima nuclear accident has driven Japanese government-led decontamination to be implemented since 2012. Within a few years, dramatic land-use changes occurred in the agricultural regions, resulting in a significant alternation in the land-ocean sediment transfer pattern. As Cs-137 can be firmly bound to minerals and transported together with river suspended sediment (SS), from the perspective of environmental sustainability, there is a need to assess whether and how these anthropogenic perturbations will cause secondary environmental impacts on downstream for long term.

Here we provide the comprehensive assessment of decontamination impacts during 2013–2018 by combining the governmental decontamination data, high-resolution satellite images, and concurrent river monitoring results. We outlined the vector decontamination map based on the official paper maps. We observed the land cover changes by drone and quantified ever-changed erosion potential (defined: KLSCP in RUSLE) in decontaminated regions based high-resolution normalized difference vegetation index (NDVI) dataset (10 m spatial resolution for ~24 km² decontaminated regions from 2011 to 2018). Besides, we also exhibited concurrent river fluctuation in water level, turbidity (temporal resolution: 10 min) and particulate Cs-137 concentrations from 2013 to 2018. With these high-resolution quantitative datasets, we systematically revealed the long-term impacts of land-use changes in decontaminated regions on upstream and downstream SS dynamics, Cs-137 particulate concentration fluctuations, downstream river SS loads, source composition, and particulate Cs-137 discharge into the Pacific Ocean.

Research sample

Our samples mainly include of three components:

- (1) High-resolution satellite images (Sentinel 2: 10 m spatial resolution; MODIS: 16 days temporal resolution) in the decontaminated regions during 2011–2018. These data were first used for generating a fusion satellite image dataset with high spatial and temporal resolution, followed by NDVI calculations, erosion potential estimation, and linear interpolation to finally establish a quantitative daily change curve of erosion potential in the decontaminated regions
- (2) Continuously recorded water levels and turbidity in upstream and downstream rivers during 2013–2018 (temporal resolution: 10 min). These data were used to study the variation of sediment loads and to explore the quantitative connection between their dynamics and quantified erosion potential changes.
- (3) Cumulatively collected suspended sediment in upstream and downstream rivers of the study basin during 2013–2018. These samples were used for river particulate Cs-137 determination, downstream Cs-137 flux estimation, and sediment source identification.

It should be noted that part of particulate Cs-137 data in the Haramachi site have been publicly available in our open-source database (<https://www.ied.tsukuba.ac.jp/database/index.html>).

Sampling strategy

In this work, we attempted to use the the highest resolution available datasets for quantifying the long-term impact of land use changes in the decontaminated regions on downstream river SS and particulate Cs-137 discharge into the ocean. For the above three sample components, our sample sizes (resolutions) were as follows.

- (1) Within the decontaminated regions (~ 24 km²), we presented the evolution of quantified erodibility with a spatial resolution of 10 m and a temporal resolution of one day for the period of 2011–2018.
- (2) Regarding the river monitoring, we conducted long-term, continuous monitoring campaign at a high temporal resolution of 10 min in the upstream (2015–2018) and downstream (2013–2018) rivers.
- (3) Regarding the Cs-137 monitoring, our passive samplers typically require a cumulative deployment of one month to collect sufficient SS sample for subsequent analysis. Compared to several years of decontamination work, monthly-level changes in river particle Cs-137 concentration could provide useful information for studying its transport behavior in the environment.

Data collection

For the above three sample components, our data collection procedures were described as follows.

- (1) B. F., A. H., and Y. Z. jointly downloaded all available Sentinel 2 and MODIS satellite images during 2011–2018 from the USGS website (<https://earthexplorer.usgs.gov/>) and NASA website (<http://reverb.echo.nasa.gov/>) for the study regions and performed subsequent analytical calculations.
- (2) W. K. and K. T. deployed water level sensors and turbidity sensors at upstream and downstream monitoring sites. They visited the site regularly (usually monthly) during 2013–2018 to download stored data and reset sensors.
- (3) W. K. and K. T. deployed cumulative suspended sediment samplers at the study area's upstream and downstream monitoring sites. They visited the site regularly (monthly in usual) during 2013–2018 to recycle the collected SS samples and re-deploy the samplers in the river.

Timing and spatial scale

For the above sample components, our data collection frequency and periodicity were described as follows:

(1) Both Sentinel 2 and MODIS satellite images were downloaded during the period of 1st January 2011 to 31st December 2018. However, only the Sentinel 2 satellite images in the period of 2016-2018 were available.

(2) The frequency of recording fluctuation in river level and turbidity was 10 minutes. At the upstream monitoring site, Notegami, the monitoring period started from 1st January 2015 to 31st December 2018. At the downstream monitoring site, Haramachi, the river was monitored from 1st January 2013 to 31st December 2018. However, the sensor damage due to the strong storm makes about 30% of turbidity data unavailable each year. Here, we estimated these missing turbidity based on concurrent water level records downstream and gave 95% confidence intervals for the estimation.

(3) The monitoring frequency of river Cs-137 is monthly in usual. The data in the upstream site, Notegami, was recorded from September 2014 to July 2017. The data in the upstream site, Warabi, was recorded from August 2014 to July 2017. The data in the downstream site, Haramachi, was recorded from December 2012 to December 2018. The data in the downstream site, Sekekawa, was recorded from August 2014 to 2017 July.

Data exclusions

Because of the strong storms, the turbidity sensors sometimes probably record an abnormal value which may introduce uncertainty in river SS load and Cs-137 flux estimation. To minimize this impact, our lab has established criteria to exclude these outliers and corrected them. More details can be found in Dr. Keisuke Taniguchi's (one of our co-authors) recent work (Scientific data, 2020; Environmental science technology, 2019).

Reproducibility

(1) For the satellite images' calculation, all results have been repeated several times and jointly confirmed by B. F., A. H., and Y. Z.

(2) We did not take measures to test the reproducibility of the river turbidity monitoring results because they were recorded concurrently, but during data processing, we verified the reliability of the results by comparing the recorded turbidity fluctuations longitudinally with the water level fluctuations and gave 95% confidence intervals for the estimated data (missing data and abnormal data).

(3) The activity of Cs-137 in suspended sediments was double-checked by our laboratory technicians, and all original samples were kept in the laboratory for periodically measurement quality checking.

Randomization

All relevant data at high resolution were recorded in our work and were used without any attendant grouping, so there were no bias in the results due to the sample allocation.

Blinding

This work did not use blinding methods. We are mainly dedicated to reveal the long-term effects of land-use changes in the decontaminated regions on the environmental sustainability of downstream river systems and this kind of environmental impact assessment does not involve randomized controlled experiments.

Did the study involve field work? Yes No

Field work, collection and transport

Field conditions

The Niida river basin (265 km²) is located about 40 km northwest of the damaged Fukushima Daiichi nuclear power plant (FDNPP). The monitoring data from the Japan Meteorological Agency shows that the average rainfall in this basin is greater than 1300 mm, with more than 75% of the rainfall occurring between May and October. According to the 3rd airborne monitoring survey by the Japanese government, the Cs-137 inventory in this region was over 700 kBq m⁻². Because of high contamination in the headwater watershed, the government-led decontamination was mainly implemented in the upstream basin from 2013 to 2016 (about 1% area extended to March 2017).

Location

River monitoring sites (water level and turbidity):

(1) Haramachi (37°39'4.28" N, 140°57'30.92"E);
(2) Notegami (37°39'45.41" N, 140°47'32.84" E)

River Cs-137 monitoring sites:

(1) Haramachi (37°39'4.28" N, 140°57'30.92"E);
(2) Notegami (37°39'45.41" N, 140°47'32.84" E);
(3) Warabi (37°36'49.10" N, 140°48'4.82" E);
(4) Sekekawa (37°38'33.70" N, 141° 0'20.36");

Access & import/export

No, our work did not include this part because all monitoring regions are fully opened.

Disturbance

No, our work did not include this part because the sizes of our sampling devices and monitoring sensors are small and their operation would not have any disturbance on local environment.

Reporting for specific materials, systems and methods

We require information from authors about some types of materials, experimental systems and methods used in many studies. Here, indicate whether each material, system or method listed is relevant to your study. If you are not sure if a list item applies to your research, read the appropriate section before selecting a response.

Materials & experimental systems

| n/a | Included in the study |
|-------------------------------------|--|
| <input checked="" type="checkbox"/> | <input type="checkbox"/> Antibodies |
| <input checked="" type="checkbox"/> | <input type="checkbox"/> Eukaryotic cell lines |
| <input checked="" type="checkbox"/> | <input type="checkbox"/> Palaeontology and archaeology |
| <input checked="" type="checkbox"/> | <input type="checkbox"/> Animals and other organisms |
| <input checked="" type="checkbox"/> | <input type="checkbox"/> Human research participants |
| <input checked="" type="checkbox"/> | <input type="checkbox"/> Clinical data |
| <input checked="" type="checkbox"/> | <input type="checkbox"/> Dual use research of concern |

Methods

| n/a | Included in the study |
|-------------------------------------|---|
| <input checked="" type="checkbox"/> | <input type="checkbox"/> ChIP-seq |
| <input checked="" type="checkbox"/> | <input type="checkbox"/> Flow cytometry |
| <input checked="" type="checkbox"/> | <input type="checkbox"/> MRI-based neuroimaging |